Direct imaging of the end-of-range and surface profiles of proton-beam written erbium-doped waveguide amplifiers by atomic force microscopy

T. C. Sum[a)]
Division of Physics and Applied Physics, School of Physical and Mathematical Sciences, Nanyang Technological University, 1 Nanyang Walk, Block 5, Level 3, Singapore 637616

A. A. Bettiol, J. A. van Kan, S. Venugopal Rao, and F. Watt
Department of Physics, Centre for Ion Beam Applications (CIBA), National University of Singapore, 2 Science Drive 3, Singapore 117542

K. Liu and E. Y. B. Pun
Department of Electronic Engineering, City University of Hong Kong, Tat Chee Avenue, Kowloon, Hong Kong

Buried channel waveguide amplifiers in erbium/ybtterbium codoped phosphate glass were fabricated using proton-beam writing. Single-mode waveguides were fabricated with fluences ranging from 0.4 to 2.0×10^{15} particles/cm^2. The end-of-range and surface profiles of the waveguides were investigated using atomic force microscopy. The waveguiding effect was investigated using the end-fire coupling technique. From the near-field mode profiles, the refractive index profiles of these waveguides were recovered using the propagation mode near-field method. From these results, it can be deduced that for phosphate glass waveguides fabricated with fluences $<1.0 \times 10^{15}$ particles/cm^2, the ionization from the electronic stopping, rather than the nuclear damage processes, is the major contributing factor leading to an increase in the refractive index near the end of range. © *2005 American Institute of Physics*. [DOI: 10.1063/1.2001748]

I. INTRODUCTION

Ion-beam irradiation has been commonly applied to modify the optical properties of a wide range of materials.[1] In the case of optical waveguide fabrication, the refractive index of a material changes after the irradiation. The refractive index profile, the degree and sign of the index change, varies considerably for different materials and is highly dose dependent. Ion-beam irradiation provides excellent controllability and reproducibility: the depth at which the optical waveguides are fabricated can be controlled by varying the ion-beam energy; the refractive index change can be accurately controlled by varying the ion-beam energy and the ion fluence. These advantages make it an attractive option for use in optical waveguide fabrication.[2–6]

Recently, we demonstrated the fabrication of erbium-doped waveguide amplifiers using proton-beam writing.[7,8] Proton-beam writing[9] is an emerging lithographic technique which employs a focused submicron beam of high-energy protons (typically 2.0 MeV), to direct write on a suitable material, such as photoresists or inorganic materials such as glasses. With its own scanning software where a variety of design file formats are supported (such as AUTOCAD™ [*].dxf), proton-beam writing can be used to fabricate any arbitrary waveguide pattern. Being a maskless technique, it is ideal for the rapid prototyping of optical circuits.

There are numerous applications for erbium-doped waveguide amplifiers[10] to compensate for signal losses in optical integrated circuits operating at 1.5 μm. Several different techniques have been employed to fabricate these Er-doped waveguide devices. These include ion exchange,[11] rf sputtering,[12] sol gel,[13] plasma-enhanced chemical-vapor deposition,[14] femtosecond laser pulses,[15] and ion irradiation.[16] Note that in the last case, Chen *et al.* fabricated planar waveguides in Er^{3+}/Yb^{3+} codoped phosphate glass using blanket irradiations with a 2.6-MeV He$^+$ beam at doses of $0.5–2 \times 10^{16}$ particles/cm^2. In contrast, proton-beam writing uses a focused microbeam of 2.0-MeV protons to direct write the buried channel waveguides at much lower doses.

In our earlier work,[7,8] we have emphasized the characterization of the optical properties of the waveguide amplifier. In this work, we report on further investigations on these waveguides using atomic force microscopy (AFM), the end-fire coupling technique, and the propagation mode near-field (PMNF) method.[17–20] Unlike fused silica, there have been very few published works[21,22] on the effects of ion-beam irradiation of phosphate glass, especially on the physical modifications over the top-face and end-of-range regions. From these results, we seek to have a better understanding of the waveguide formation mechanism of proton-beam written IOG-1 phosphate glass waveguide amplifiers.

II. EXPERIMENT

A. Waveguide fabrication

In this work, the substrates used were the commercially available IOG-1 phosphate laser glass codoped with Er (2.2 wt %) and Yb (4.7 wt %) ions (Schott Glass Technologies Inc.). IOG-1 is a sodium-aluminum-phosphate-based glass developed for active waveguide fabrication[23] using po-

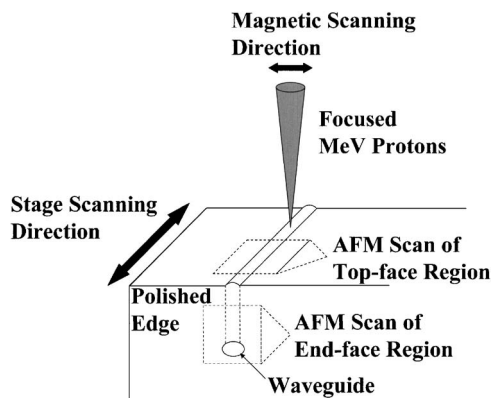[a)]Author to whom correspondence should be addressed; electronic mail: tzechien@ntu.edu.sg

FIG. 1. A schematic showing the directions of the stage and magnetic scannings, as well as the relative locations of the waveguide top face and the end face.

FIG. 2. DIC micrograph of a trio of linear waveguides spaced 400 μm apart. Inset shows a DIC micrograph of the cross section of one of the waveguides fabricated with a fluence of 3×10^{15} particles/cm^2.

tassium and silver ion exchange. The samples with a thickness ~1.6 mm were cut into pieces approximately 10 × 10 mm (length × breadth), which were edge polished prior to the direct write. Proton-beam writing is carried out using proton beams from the High Voltage Engineering Europa (HVEE) 3.5-MeV Singletron™ accelerator at the Centre for Ion Beam Applications (CIBA),[24] National University of Singapore. The waveguides were direct written using a 2.0-MeV beam of protons with a beam spot size of ~1.0 μm and a beam current of ~100 pA. The protons were focused using magnetic quadrupole lenses.[25] Based on the stopping and range of ions in matter[26] (SRIM) simulations, 2.0-MeV protons have a range of approximately 38 μm in the phosphate laser glass. The IOG-1 phosphate laser glass were irradiated with proton doses ranging from 0.4 to 6.0×10^{15} particles/cm^2.

A combination of stage scanning and magnetic scanning was used to direct write the waveguides. The sample was mounted on a three-axis computer-controlled piezoelectric translational stage (Burleigh TSE-150HV Integral Encoder Stage). The proton beam was magnetically scanned over a distance of 5 μm in one direction, while simultaneously the stage was traversed perpendicular to this magnetic scan direction at a speed of ~2 μm/s. A schematic of the geometry of the proton-beam writing direction is shown in Fig. 1. Multiple stage scans in the forward and reverse directions were performed to ensure that the dose is uniform over the entire length of the waveguide. A more detailed description of the magnetic scanning procedure and the dose normalization procedure can be found elsewhere.[27]

B. AFM measurements

After the irradiations, the surfaces of the waveguide top faces and end faces were imaged using an atomic force microscope (AFM)—Digital Instruments Dimension™ 3000 SPM. The AFM was operated in tapping mode using an etched silicon cantilever with a length of 125 μm, with a nominal tip radius of curvature of approximately 5–10 nm. A schematic of the approximate locations of the AFM scans are given in Fig. 1. The samples were then thermally an-
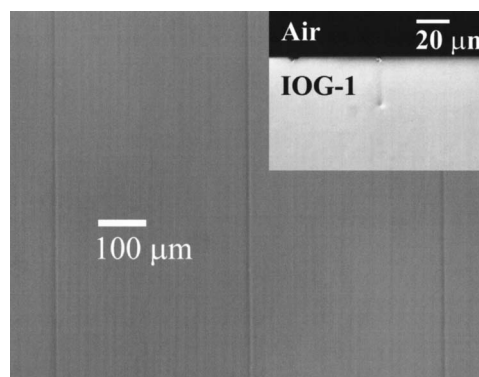
nealed at 220 °C for 30 min. The AFM scans over the top faces and end faces were again performed after the thermal annealing.

C. Near-field measurements

The waveguiding effect was investigated using the end-fire coupling technique and near-field mode profiles at 632.8-nm wavelength were imaged using a 50× long working distance microscope objective (NA=0.42, resolving power ~0.7 μm) mounted on an InfiniTube™ in-line assembly and connected to a 12-bit charge-coupled device (CCD) camera—Q-Imaging™ RETIGA EXi Digital CCD Camera. The refractive index profiles of the single-mode PMMA buried channel waveguides were also recovered using the propagation mode near-field method (also known as the scalar wave inversion technique).

III. RESULTS

A. Measurement of surface swelling using an AFM

Figure 2 shows the differential interference contrast (DIC) image of an overview of the fabricated waveguides. The inset shows a cross-sectional view of the end face of one of the waveguides. A contour plot of a typical AFM scan of a postannealed waveguide end face is given in Fig. 3. The
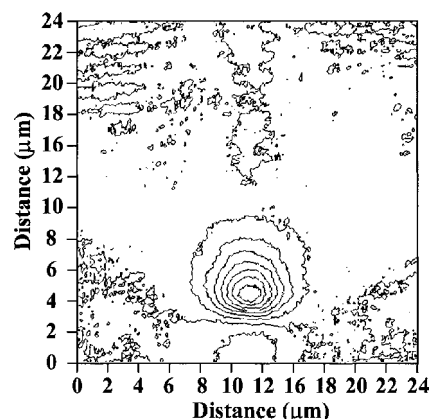

FIG. 3. Contour plot of a waveguide end face imaged using an AFM to illustrate the swelling in the phosphate glass. The height per contour line is ~3.47 nm. The waveguide was fabricated using 3×10^{15} particles/cm^2.
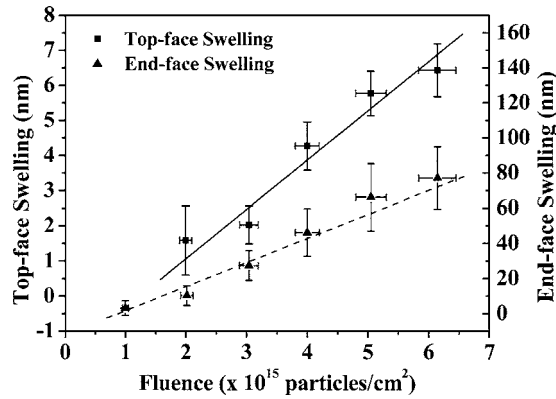
FIG. 4. A plot of the variation of the top-face and end-face swelling of the waveguides as a function of proton fluence.

FIG. 5. Near-field mode profiles of *p*-beam written waveguides fabricated with fluences of approximately (a) 0.4×10^{15}, (b) 1.0×10^{15}, (c) 2.0×10^{15}, and (d) 3.0×10^{15} particles/cm^2. The dotted line indicates the approximate location of the end of range. (e) A schematic illustrating the stress buildup (dotted arrows). Inset shows the mode profile.

root-mean-square (rms) surface roughnesses of the polished edges and sample top face were also measured and were found to be ~2.23 and ~1.87 nm, respectively, over an area of 30×30 μm^2. The AFM images were flattened using a low-order polynomial fit. Such manipulation of raw AFM data is usually performed to remove the image artifacts (such as vertical offsets between scan lines), which may be caused by vertical (Z) scanner drift, image bow, or any nonlinear behavior in the piezoscanning mechanism.

Both preannealed and postannealed top face and end face swelling profiles were imaged using the AFM. However, no significant reduction of the swelling is observed between the two data sets. Figure 4 shows the variation of the postannealed top-face and end-face swelling of the waveguides as a function of proton fluence. The AFM data on the postannealed top-face and end-face swelling profiles show that the swelling increases as a function of proton fluence. Both data sets were fitted using a linear least-square fit. The uncertainty in the measured values of the swelling is attributed to the differences in the processed AFM data (caused by the flattening procedure) and the variation in the surface roughness. Below a fluence of ~2.0×10^{15} particles/cm^2 for the top face and a fluence of ~1.0×10^{15} particles/cm^2 for the end face, the surface roughness of the respective surfaces is comparable to the swelling. Hence, it is not possible to measure the swelling (if any) on these surfaces for fluences below these values.

B. Near-field mode profiles

From the end-fire coupling measurements, it was found that at 632.8-nm wavelength, light guidance near the end of range is supported for waveguides fabricated using fluences up to 2.0×10^{15} particles/cm^2. Figures 5(a)–5(c) show several typical mode profiles of the proton-beam written waveguides. Vertical line scans of the mode profiles were also extracted and compared with the SRIM simulations of the electronic energy deposition and the atomic displacements (Fig. 6). Analysis of the mode profiles reveals that the peak intensity is located at a distance approximately $\geqslant 3$ μm before the end of range. The structure in the mode profile between the end of range and the surface of the structure is believed to be a consequence of the interference due to scat-
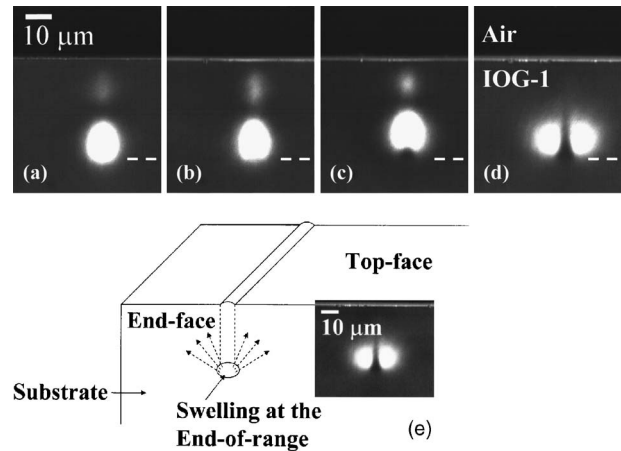
tered light being reflected from the surface of the substrate. For fluences $> 3.0 \times 10^{15}$ particles/cm^2, a "nonwaveguiding" channel, as shown in Fig. 5(d), is formed. The light is observed to be propagating "outside" the channel and along both its sides. The typical "teardrop" ion implantation profile is clearly visible. In addition, no light confinement in the region beneath the end of range is observed.

C. Refractive index profile reconstruction

The refractive index profiles of the single-mode waveguides (i.e., waveguides fabricated with fluences $< 1 \times 10^{15}$ particles/cm^2) were recovered using the PMNF method,[17–20]

$$\Delta n(x,y) = - \frac{\nabla^2 \sqrt{I(x,y)}}{2 n_s k_0^2 \sqrt{I(x,y)}}, \qquad (1)$$

where n_s refers to the substrate refractive index, k_o is the free space wave number, and $I(x,y)$ is the normalized intensity.
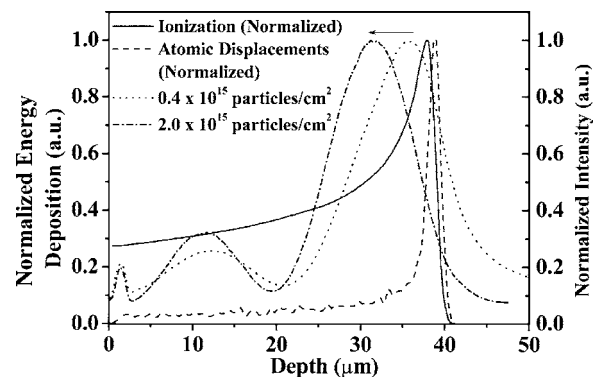

FIG. 6. A plot of the intensity profiles for two different fluences. As the fluence increases, the intensity peak shifts towards shallower depths (solid horizontal arrow). The normalized energy deposition due to the electronic energy deposition (solid line) and atomic displacements (dashed line) from the SRIM simulations are also plotted to indicate the approximate location of the end of range.
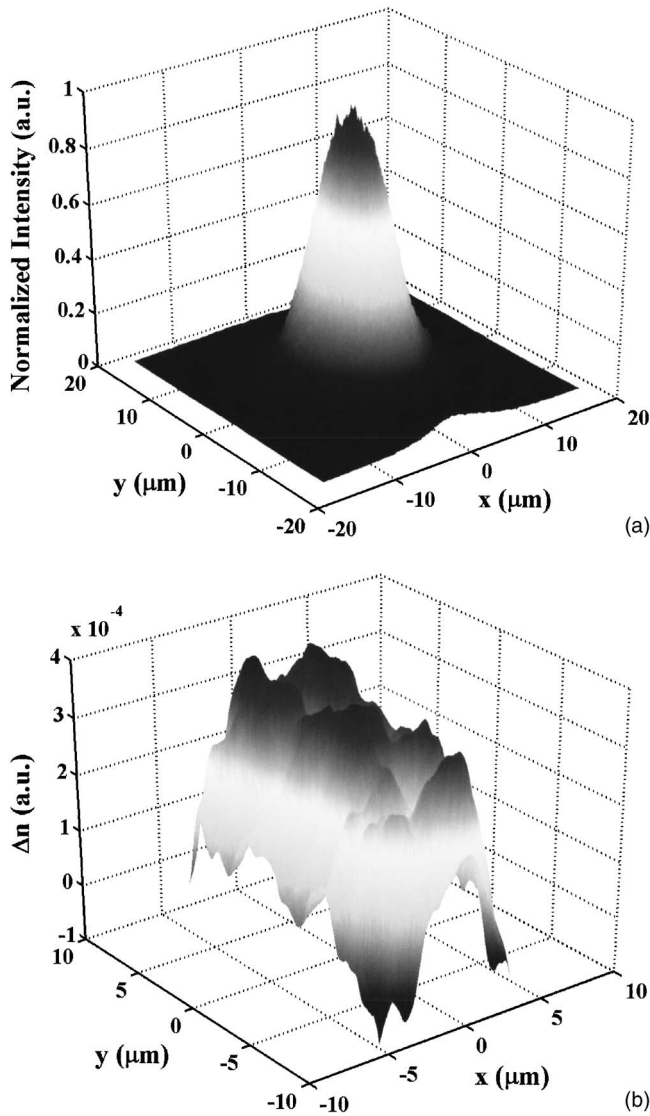
FIG. 7. (a) Normalized single-mode near-field profile (at 632.8-nm wavelength) of a proton-beam written IOG-1 waveguide fabricated using a fluence of ~0.4×10¹⁵ particles/cm². (b) The recovered Δn of the same waveguide.

The second-order derivatives found in Eq. (1) require good mode profile data with low noise. Averaging of the mode profiles and maximizing the signal to noise ratio by exposing the CCD array for as long as possible without saturating the CCD pixels were some of the precautions taken. In addition, the average image of the mode profile was filtered using a Butterworth low-pass filter with a transfer function of $H(w) = \sqrt{1/(1+w^4)}$. A MATLAB™ (The MathWorks Inc.) program was written to perform the necessary low-pass filtering and the subsequent recovery of the refractive index profile $\Delta n(x,y) = n(x,y) - N_{eff}$. The PMNF technique was first tested on a commercial fiber (3M FSSN-3224 single-mode fiber) and the recovered refractive index profile was found to be in good agreement with the manufacturer's specifications.

The bulk refractive index n_s of pristine IOG-1 phosphate glass was measured using a prism coupler and was found to be 1.522 at 632.8-nm wavelength. The normalized intensity profile of a guide fabricated with a fluence of ~0.4 ×10¹⁵ particles/cm² is shown in Fig. 7(a) and the recovered
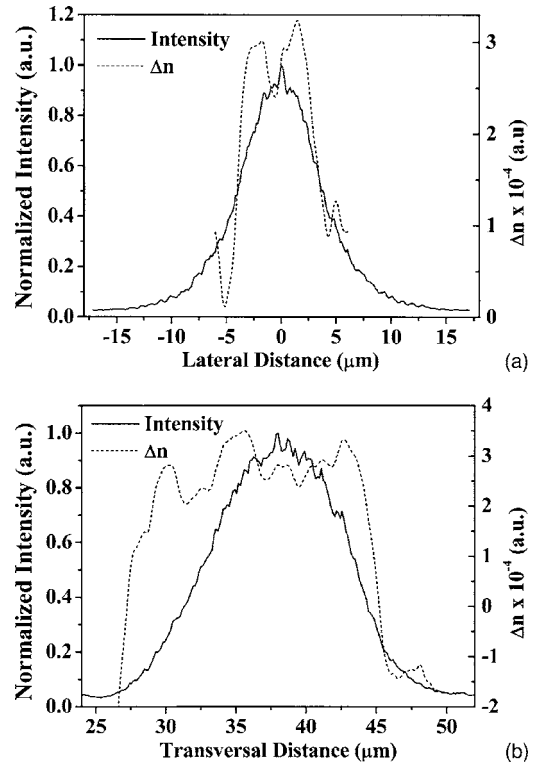

FIG. 8. (a) A 2D lateral plot of the normalized intensity (solid) and the recovered profile (dashed). (b) A 2D transversal (depth) plot of the normalized intensity (solid) and the recovered profile (dashed).

index change (Δn) is given in Fig. 7(b). These results verify that the proton irradiation has caused an increase of the refractive index (i.e., $\Delta n > 0$) near the end of range. The two-dimensional (2D) lateral and depth plots of the normalized intensity and the recovered profile are given in Figs. 8(a) and 8(b). The peak refractive index change of the IOG-1 phosphate glass waveguides fabricated using fluences of ~0.4–1.0×10¹⁵ particles/cm² ranges from ~3.2 to 3.7 ×10⁻⁴. The Δn as a function of fluence was plotted in Fig. 9. These results show that the mechanism for waveguide fabrication is different from that of the "optical barrier" concept of fabricating planar waveguides previously reported[11,16] where the light is confined in the region between the barrier and the top surface of the material. Note that the refractive index of this region is higher than that of the barrier but lower than the unmodified substrate.
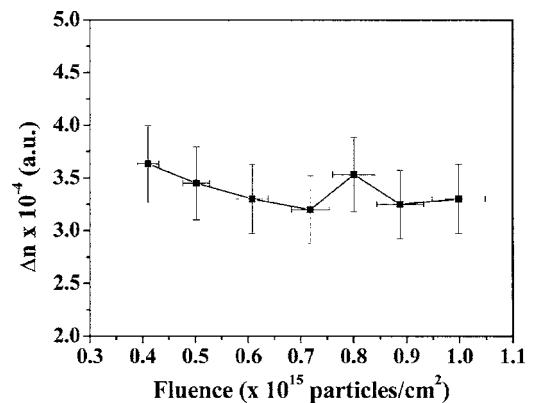

FIG. 9. A plot of the recovered refractive index change (Δn) against proton fluence.

IV. DISCUSSION

In the case of ion implantation, one of the dominant factors contributing to the refractive index change of a material is due to the nuclear damage processes.[22] Near the end of range, where the proton has been considerably slowed down, collision events between the incident ion and the target nuclei become more probable. For many materials, this "damage" often result in changes in the physical density (i.e., change in volume, ΔV) leading to the changes in the refractive index Δn. In addition to ΔV, there are other defect-dependent parameters such as the atomic bond polarizability ($\Delta \alpha$) and the structure factor (F). The relationship between Δn and these defect-dependent parameters are described by the Wei adaptation of the Lorentz-Lorenz equation,[28]

$$\frac{\Delta n}{n} = \frac{(n^2 - 1)(n^2 + 2)}{6n^2}\left[-\frac{\Delta V}{V} + \frac{\Delta \alpha}{\alpha} + F\right]. \quad (2)$$

There are very few published works on the effects of proton irradiation of phosphate glass. Matsunami *et al.*[21] previously investigated the effects of modifying magnesium phosphate glass using 120-keV H$^+$ irradiation. It was reported that O–H bonds break due to electronic energy deposition by ions at low fluences—i.e., $<10^{17}$ particles/cm^2. At higher fluences (i.e., $>10^{17}$ particles/cm^2), the reduction of PO$_4$ tetrahedron to P colloid overcomes O–H bond breaking due to interaction of the H$^+$ with the substrate, resulting in the formation of P–OH and H$_2$O.

From our AFM data, at fluences $<1.0 \times 10^{15}$ particles/cm^2, no measurable volume change (i.e., swelling/compaction) near the end of range can be detected. At these fluences, the near-field mode profiles of these waveguides show that there is good mode confinement in the channel. The modes are confined at the region before the end of range (where most of the atomic displacements are produced). The refractive index profiles of these (single mode) waveguides recovered using the PMNF technique confirmed that an increase in the refractive index (i.e., $\Delta n > 0$) has occurred. These results indicate that the phosphate waveguides formed at these fluences may not be attributed entirely to the nuclear damage process which changes the volume (i.e., ΔV). This is contrary to that reported for fused silica,[29] where the refractive index increase is caused by compaction of the material, resulting in a decrease in volume (i.e., $\Delta V < 0$) and increasing the density in the process. The absence of any measurable volume change for the waveguides irradiated with fluences $<1.0 \times 10^{15}$ particles/cm^2 may be attributed to the competing effects of the bond-breaking and bond-forming processes described above. In view of this interpretation, it is very likely that the contributions from $\Delta \alpha$ or F or both [see Eq. (2)] may have a greater effect on the refractive index increase rather than ΔV. Further work using the Fourier transform Raman (FT-Raman) technique may be needed to determine the relative contributions of these effects to the refractive index increase.

From the AFM data, the swelling of the waveguide end faces and top faces becomes appreciable at fluences $>1.0 \times 10^{15}$ and 2.0×10^{15} particles/cm^2, respectively. The amount of swelling in the end face compared to the top face
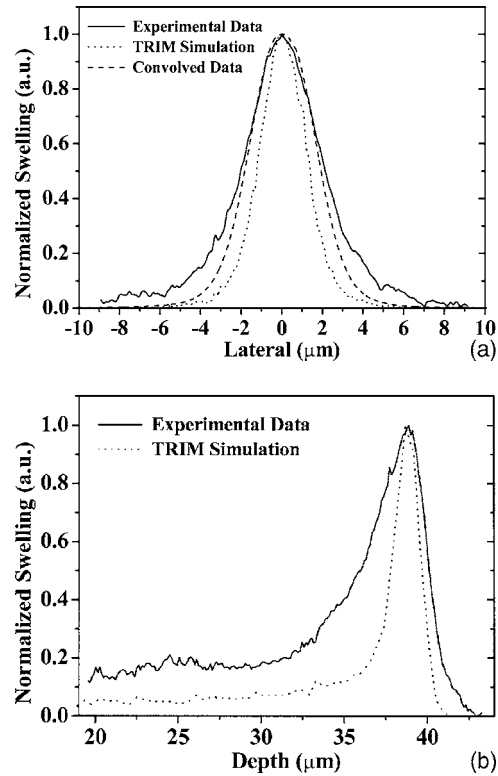

FIG. 10. A comparison of the lateral swelling profile (solid) with the atomic displacements simulated using TRIM (dotted). The data from the TRIM simulation were convoluted with a Gaussian beam profile with a beam spot size of 1 μm and a scan size of 5 μm (dashed). (b) A comparison of the vertical swelling profile (solid) with the atomic displacements simulated using TRIM (dotted).

of the waveguide is much more pronounced (at least a factor of 10 times based on the comparison of the gradients of both linear fits). The thermal annealing step which does not seem to have much effect on the swelling profiles is probably essential for the removal of the color center absorption[21] as the average propagation losses of these phosphate glass waveguides were reduced[7] after the thermal annealing step.

The lateral and depth swelling profiles (i.e., profiles perpendicular and parallel to the ion path, respectively) of one of the waveguides (fluence $\sim 3.0 \times 10^{15}$ particles/cm^2) are compared with the atomic displacement profiles predicted by SRIM [Figs. 10(a) and 10(b)]. In the former case, the swelling profile is wider than that simulated using SRIM since SRIM assumes a beam of protons of infinitesimal spot size. A more realistic comparison would involve a convolution of the SRIM simulation with a Gaussian beam with a beam spot size of 1 μm and the magnetic scan size of 5 μm. The resultant convolved profile is also plotted in Fig. 10(a). It can be seen that the convolved data provide a more realistic modeling of the swelling profile. However, the slight mismatch between the convolved data and the experimental data, especially at the regions beyond the full width half maximum (FWHM), may be attributed to deformation of the surface due to the swelling. This accumulated stress may be responsible for increasing the density of the phosphate glass at regions external to the channel, resulting in an increase in the refractive index, permitting light confinement, as shown in Fig. 5(d).

However, it is unclear why no waveguiding is observed for regions beyond the end of range.

In the case of the depth profile as shown in Fig. 10(b), the swelling profile is wider than that simulated using SRIM. Unlike the previous case, parameters such as the finite size of the beam do not contribute to the depth profile. From the plot, the atomic displacements only partially account for the width of the depth swelling profile at the end of range. The additional contribution may be attributed to the ionization processes[21] that dominate in the region between the surface and the end of range which causes structural modification. Further work on this is required to determine the extent of the contributions from the ionization processes on the depth swelling profile for this IOG-1 phosphate glass.

For fluences $>3.0\times10^{15}$ particles/cm^2, a nonwaveguiding channel, as shown in Fig. 5(d), is formed. There are two possible explanations for this observation. One possible interpretation is that the threshold irradiation fluence has being exceeded, causing the refractive index within the ion track or the end-of-range region to be lower than the surrounding regions. The AFM data show an appreciable amount of end-face swelling (i.e., $\Delta V > 0$) at fluences $>3.0 \times 10^{15}$ particles/cm^2 ($\sim$30 nm). This swelling is most likely attributed to the bond-formation processes discussed earlier and from Eq. (1), a decrease in the refractive index ($\Delta n < 0$) within the channel will result. As shown in Fig. 6, unlike the atomic displacement profile which peaks at the end of range ($\sim$38 μm), the ionization profile gradually increases and has a much broader profile. The peaks in the intensity profile are shallower than both the modal depth of ionization and atomic displacement damage as predicted by SRIM (Fig. 6). This could be a consequence of the reduction of the change in refractive index by ionization, while atomic displacement leads to swelling and hence Δn becomes reduced. This explanation is consistent with the shift in the peak intensity [Fig. 5(e)] with increasing fluence. The light confinement at regions external to the irradiated region (just above the end of range) may be attributed to the density increase caused by the builtup of stress due to the swelling. The stress buildup is possibly directed upwards and towards the top surface, as indicated in Fig. 5(e).

Alternatively, Fig. 5(d) may also be interpreted as the mode profile of a multimode waveguide. From the optical fiber theory, the number of allowed modes[30] for a circular waveguide is approximately given by

$$N \approx \frac{a^2}{2}\left(\frac{2\pi}{\lambda}\right)^2 (2n \cdot \Delta n), \tag{3}$$

where a is the radius of the fiber core, n is the refractive index of the core, and Δn is the change in refractive index between the core and the cladding. From Eq. (3), the number of modes for a circular waveguide increases as the refractive index change increases. Hence, it is highly possible that as the proton fluence increases, the change of refractive index increases, thus forming a multimode waveguide. The "misshapen" mode shown in Fig. 5(c) may be an indication of the onset of a gradual transition from a single-mode waveguide to a multimode waveguide. Unfortunately, the PMNF method can only be used to recover the refractive index pro-

files of single-mode waveguides. To establish the actual cause for the mode profiles observed in Figs. 5(c) and 5(d), further work using the refracted near-field (RNF) technique[31] is needed to measure the refractive index profiles of these multimode waveguides.

V. CONCLUSIONS

In summary, the end-of-range and surface profiles of proton-beam written waveguides in IOG-1 phosphate glass were imaged using an AFM. End-fire coupling was also performed and the near-field mode profiles of the waveguides were imaged. The refractive index profiles of the single-mode waveguides were recovered using the propagation mode near-field method. From these results, it can be deduced that for waveguides fabricated using fluences $<1.0 \times 10^{15}$ particles/cm^2, the nuclear damage processes are not the major contributing factors leading to $\Delta n > 0$ near the end of range. It is plausible that the ionization has a significant contribution on the refractive index increase. This work has also demonstrated that buried channel waveguide amplifiers in phosphate glass can be fabricated using ion implantation at much lower doses. The mechanism for waveguide fabrication is different from that of the "optical barrier" concept of fabricating planar waveguides previously reported[11,16] where much higher ion doses are required. To get a better understanding of the waveguide formation mechanism in phosphate glass, further work using FT-Raman measurements to investigate the ion-matter interactions in phosphate glass and the RNF measurements to investigate the refractive index profiles of multimode waveguides are needed.

[1]P. D. Townsend, Vacuum **51**, 301 (1998).
[2]T. C. Sum, A. A. Bettiol, H. L. Seng, I. Rajta, J. A. van Kan, and F. Watt, Nucl. Instrum. Methods Phys. Res. B **210**, 266 (2003).
[3]S. García-Blanco, A. J. Kellock, J. E. E. Baglin, A. Glidle, J. M. Cooper, J. S. Aitchison, and R. M. De La Rue, Nucl. Instrum. Methods Phys. Res. B **206**, 440 (2003).
[4]D. M. Ruck, Nucl. Instrum. Methods Phys. Res. B **166–167**, 602 (2000).
[5]M. L. von Bibra, A. Roberts, and S. D. Dods, Nucl. Instrum. Methods Phys. Res. B **168**, 47 (2000).
[6]P. Sreeramana Aithal, H. S. Nagaraja, P. Mohan Rao, V. P. N. Nampoori, C. P. G. Vallabhan, and D. K. Avasthi, Nucl. Instrum. Methods Phys. Res. B **129**, 217 (1997).
[7]K. Liu, E. Y. B. Pun, T. C. Sum, A. A. Bettiol, J. A. van Kan, and F. Watt, Appl. Phys. Lett. **84**, 684 (2004).
[8]T. C. Sum, A. A. Bettiol, K. Liu, M. Q. Ren, E. Y. B. Pun, S. Venugopal Rao, J. A. van Kan, and F. Watt, Nucl. Instrum. Methods Phys. Res. B **231**, 394 (2005).
[9]T. C. Sum, A. A. Bettiol, J. A. van Kan, F. Watt, E. Y. B. Pun, and K. K.

Tung, Appl. Phys. Lett. **83**, 1707 (2003).

[10]G. N. van den Hoven, R. J. I. M. Koper, A. Polman, C. van Dam, J. W. M. van Uffelen, and M. K. Smit, Appl. Phys. Lett. **68**, 1886 (1996).

[11]S. F. Wong, E. Y. B. Pun, and P. S. Chung, IEEE Photonics Technol. Lett. **14**, 80 (2002).

[12]P. G. Kik and A. Polman, J. Appl. Phys. **93**, 5008 (2003).

[13]W. Huang, R. R. A. Syms, E. M. Yeatman, M. M. Ahmad, T. V. Clapp, and S. M. Ojha, IEEE Photonics Technol. Lett. **14**, 959 (2002).

[14]H. S. Han, S. Y. Seo, J. H. Shin, and N. Park, Appl. Phys. Lett. **81**, 3720 (2002).

[15]J. W. Chan, T. R. Huser, S. H. Risbud, J. S. Hayden, and D. M. Krol, Appl. Phys. Lett. **82**, 2371 (2003).

[16]F. Chen, X. L. Wang, X. S. Li, L. L. Hu, Q. M. Lu, K. M. Wang, B. R. Shi, and D. Y. Shen, Appl. Surf. Sci. **193**, 92 (2002).

[17]K. Morishita, J. Lightwave Technol. **LT1**, 445 (1983).

[18]K. Morishita, J. Lightwave Technol. **LT4**, 1120 (1986).

[19]G. L. Yip, P. C. Noutsios, and L. Chen, Appl. Opt. **35**, 2060 (1996).

[20]M. L. von Bibra and A. Roberts, J. Lightwave Technol. **15**, 1695 (1997).

[21]N. Matsunami, K. Kawamura, and H. Hosono, Radiat. Eff. Defects Solids **136**, 311 (1995).

[22]P. D. Townsend, P. J. Chandler, and L. Zhang, in *Optical Effects of Ion Implantation*, edited by P. L. Knight and A. Miller (Cambridge University Press, Cambridge, 1994), Vol. 13, Chap. 6, p. 199.

[23]D. L. Veasey, D. S. Funk, N. A. Sanford, and J. S. Hayden, Appl. Phys. Lett. **74**, 789 (1999).

[24]F. Watt, J. A. van Kan, I. Rajta, A. A. Bettiol, T. F. Choo, M. B. H. Breese, and T. Osipowicz, Nucl. Instrum. Methods Phys. Res. B **210**, 14 (1997).

[25]G. W. Grime and F. Watt, in *Principles and Application of High-Energy Ion Microbeams*, edited by F. Watt and G. W. Grime (IOP, London, 1987), Chap. 3, p. 3.

[26]J. F. Ziegler, J. P. Biersack, and U. Littmark, *Stopping and Range of Ions in Matter* (Pergamon, New York, 1985).

[27]A. A. Bettiol, J. A. van Kan, T. C. Sum, and F. Watt, Nucl. Instrum. Methods Phys. Res. B **181**, 49 (2001).

[28]K. Wenzlik, J. Heibei, and E. Voges, Phys. Status Solidi A **61**, 207 (1980).

[29]M. L. von Bibra, A. Roberts, P. Mulvaney, and S. T. Hungtington, J. Appl. Phys. **87**, 8429 (2000).

[30]Jasprit Singh, *Optoelectronics: An Introduction to Materials and Devices* (McGraw-Hill, New York, 1996), Chap. 3, p. 106.

[31]R. Goring and M. Rothhardt, J. Opt. Commun. **7**, 82 (1986).